DETECTION BY SPACE-BORNE AND GROUND-BASED LIDAR OBSERVATIONS OF AIR POLLUTION ON THE EXAMPLE OF THE HEFEI AREA**

Hao Yang [1,2,3], Zh. Fang [1,2,3], X. Deng [1,2,3], Y. Cao [1,2,3], Ch. Xie [1,3]*

[1] Key Laboratory of Atmospheric Optics, Anhui Institute of Optics and Fine Mechanics, Chinese Academy of Sciences, Hefei 230031, China; e-mail: cbxie@aiofm.ac.cn
[2] Science Island Branch of Graduate School, University of Science and Technology of China, Hefei 230026, China
[3] Advanced Laser Technology Laboratory of Anhui Province, Hefei 230037, China

Severe air pollution is a serious threat to public health in the Yangtze River Delta region, where high concentrations of particulate matter are often observed in winter. In the present study, a serious aerosol pollution incident in the western Yangtze River Delta, China, was investigated by using joint inversion of CALIPSO and ground-based lidar in Hefei during 17–22 January, 2019. The data of the past two years were used in this study, and four typical weather cases were selected for comparative verification—namely, fine weather (less cloud, good air); cloudy weather (good air, no haze); moderate pollution weather (moderate haze, no cloud); and severe pollution weather (heavy haze, cloud). The vertical profile of aerosol backscatter as the satellite passed through Hefei city was given by the data of the CALIPSO satellite-borne lidar, CALIOP, which was compared with the vertical distribution of the range-corrected signal of ground-based lidar. Combined with analysis of meteorological data, the results showed that satellite–ground lidar can be used to observe the effect of aerosol changes on weather effectively. Subsequent experiments observed and tracked severely polluted weather event, and the data on the aerosol boundary layer was obtained which was a severe trans-boundary air pollution. The serious pollution period occurred from 22:00 to 04:00 on January 19 to 20, 2019, when the aerosol boundary layer was at its lowest (less than 0.5 km) and the boundary layer height ranged from 0.5 km to 2.2 km in other periods. Then, based on analysis of near-surface data, the changes in the boundary layer during the pollution process and the possible causes of these changes were analyzed. It was concluded that, during the pollution process, the height of the aerosol boundary layer in the Hefei area showed an obvious negative correlation with the concentration of $PM_{2.5}$. Finally, HYSPLIT results showed that the source of pollution weather was mainly aerosol particles blown from the north. The results of this study provide a basis for satellite- and ground-based lidar joint observation under different weather types, as well as help in the study of urban weather change and pollution prevention.

Keywords: *CALIPSO, Raman–Mie lidar, air pollution, aerosol boundary layer.*

ОБНАРУЖЕНИЕ С ПОМОЩЬЮ КОСМИЧЕСКИХ И НАЗЕМНЫХ ЛИДАРНЫХ НАБЛЮДЕНИЙ ЗАГРЯЗНЕНИЯ ВОЗДУХА

Hao Yang [1,2,3], Zh. Fang [1,2,3], X. Deng [1,2,3], Y. Cao [1,2,3], Ch. Xie [1,3]*

УДК 551.510.42

[1] Аньхойский институт оптики и точной механики Китайской академии наук, Хэфэй 230031, Китай; e-mail: cbxie@aiofm.ac.cn
[2] Университет науки и техники Китая, Хэфэй 230026, Китай
[3] Лаборатория передовых лазерных технологий провинции Аньхой, Хэфэй 230037, Китай

(Поступила 11 декабря 2020)

Сильное загрязнение воздуха представляет собой серьезную угрозу для здоровья населения. Эпизод с аэрозольным загрязнением в западной части дельты реки Янцзы (Китай) рассмотрен с помощью совместной инверсии CALIPSO и наземного лидара в городе Хэфэе в период 17–22 января 2019 г.

**Full text is published in JAS V. 88, No. 6 (http://springer.com/journal/10812) and in electronic version of ZhPS V. 88, No. 6 (http://www.elibrary.ru/title_about.asp?id=7318; sales@elibrary.ru).

Из данных за последние два года для сравнительной проверки выбраны четыре типичных погодных случая: хорошая погода (меньше облачности, хороший воздух); пасмурная (хороший воздух, отсутствие дымки); умеренная загрязненная (умеренная дымка, без облачности); погода с сильным загрязнением (сильная дымка, облачность). Вертикальный профиль обратного рассеяния аэрозоля получен по данным спутникового лидара CALIOP (CALIPSO) при прохождении спутника над городом Хэфэй, которые сравнивались с вертикальным распределением скорректированного по дальности сигнала наземного лидара. Показано, что комбинацию спутникового и наземного лидаров можно использовать для эффективного наблюдения за влиянием аэрозольных изменений на погоду. Последующие эксперименты отслеживали погодные явления с сильным загрязнением. Получены данные о пограничном слое аэрозоля, который представляет собой серьезное трансграничное загрязнение воздуха. Период серьезного загрязнения — с 22:00 до 04:00 19–20 января 2019 г., когда граничный слой аэрозоля находится на самом низком (<0.5 км) уровне, в другие периоды высота пограничного слоя 0.5—2.2 км. С учетом приповерхностных данных проанализированы изменения пограничного слоя в процессе загрязнения и их возможные причины. Сделан вывод о том, что во время загрязнения высота пограничного слоя аэрозоля в районе Хэфэя имеет очевидную отрицательную корреляцию с концентрацией $PM_{2.5}$. Согласно результатам HYSPLIT, основной источник загрязнения — аэрозольные частицы, уносимые с севера. Результаты дают основу для использования совместных спутниковых и наземных лидарных наблюдений при изучении изменения погоды в городах и предотвращения загрязнения атмосферы.

Ключевые слова: *CALIPSO, лидар Рамана–Ми, загрязнение воздуха, аэрозольный пограничный слой.*

Introduction. Aerosol is composed of solid or liquid particles suspended in the atmosphere, and has direct and indirect effects on weather and climate change [1–5]. In addition, due to the extinction of aerosols, visibility can be directly affected, which has an important impact on transportation, navigation, military operations, and so on [5, 6]. In particular, aerosol particles can have a serious impact on public health, especially by causing respiratory diseases [5]. In recent years, with the acceleration of urbanization and the rapid socioeconomic development, China has experienced intensive industrial emissions, the combustion of fossil fuels and the increase of vehicle emissions. Due to the small particle size and long life of anthropogenic aerosols in many areas, these have a significant impact on the atmospheric environment [4–9]. In addition to sustained emissions, the distribution of aerosol in China is also closely related to certain weather patterns, and there is a significant correlation between the change in aerosol concentration and many meteorological variables, including mixing-layer height, temperature, wind speed, relative humidity and visibility [10–15]. Significant seasonal variations in aerosols have been reported in a number of studies in China, partly due to the transport of aerosols by different wind directions during the winter and summer monsoons [16–20]. In particular, studies have shown that understanding the vertical distribution of boundary layers and aerosols is crucial to explain changes in aerosol concentrations on the ground, especially observations and studies of air pollution under the influence of trans-boundary transport, indicating that the aerosol concentrations measured at ground level are closely related to the vertical profile of aerosol [18–21]. However, different pollution sources, underlying surfaces and land-use types have different effects on the vertical distribution of aerosol. Especially in areas with high-density cities, e. g., city clusters in the Yangtze River Delta Region (YRDR), our understanding of the vertical distribution of aerosols is very limited. Therefore, more observations on the vertical distribution and spatial variation of aerosols are needed in the YRDR.

In aerosol detection, lidar has developed into a very important technology, because the laser beam emitted by lidar can interact with aerosol and cloud particles, and the vertical profile at high resolution can be obtained by receiving the backscatter signal of the lidar, meaning it can observe the optical properties and vertical spatial distribution of aerosols [21–28]. Ground-based lidar can be observed at a fixed point for a long time, with high detection accuracy, but limited observation range, and can only detect aerosol distribution characteristics at a one-dimensional vertical height. However, space-borne lidar has the advantages of a wide detection range, high resolution, effective identification of cloud components, determination of aerosol layers, and identification of aerosol types. To date, many scientists have used the observational data of the CALIPSO satellite and ground-based data for verification research. The CALIPSO satellite mainly carries three payloads: a lidar (CALIOP), an infrared radiation imager (IIR), and a wide-angle camera (WFC). Based on extensive comparisons with ground-based lidar systems in several countries, CALIOP has generally shown good performance and design expectations [24, 26, 29, 30]. Therefore, the combination of detec-

tion with satellite and earth lidar can capture effectively the three-dimensional spatial and temporal distribution characteristics of aerosols [29–32], especially for the process of weather-scale heavy pollution.

The YRDR is one of the areas in China with the most severe aerosol pollution. Hefei, as an important bridgehead for the economic development of the western part of the Yangtze River Delta city cluster, has attracted the attention of scientists in recent years owing to its worsening pollution [19, 33]. In particular, ground-based lidar monitoring in the western suburbs of Hefei plays an important role in monitoring air pollution in the western Yangtze River Delta [25, 33, 34]. On 17–22 January 2019, a heavy pollution process occurred in Hefei, which was completely captured by lidar. Based on ground-based lidar, combined with the data of CALIOP and ground meteorological data, this paper explores this heavy pollution process and its causes in the western YRDR. In Section 2, the range-corrected signal is given. In Section 3, a case study of four typical weather conditions jointly observed by satellite-based and ground-based lidars is introduced. In Section 4, the general characteristics of vertical aerosol, local meteorological conditions, the aerosol boundary layer, airmass motion, and air-pollutant concentrations are summarized. Finally, a conclusion is given in Section 5.

Data and methods. *Lidar data.* Ground-based lidar data were obtained from Raman–Mie lidar developed by the Anhui Institute of Optics and Fine Mechanics, Chinese Academy of Sciences. Figure 1 shows a schematic diagram of its system configuration. The Raman–Mie lidar has six acquisition channels with three wavelengths (1064, 532, and 355 nm) for observation and acquisition. The vertical resolution is 7.5 m and the observation point (31.90°N, 117.16°E) is continuously observed for 24 h. Table 1 compares the main technical parameters of CALIOP and the Raman–Mie lidar. In addition, in this study, the 532-nm backscattering coefficient profile data from CALIOP's Level 1B classification were used. CALIOP is a dual-wavelength (1064 and 532 nm) polarized lidar system (three echo channel signals with cross-polarization components of 1064-nm backscattering and 532-nm backscattering) [25, 26, 31]. CALIOP has a vertical resolution of 30 m below 8 km, a horizontal resolution of 333 m, and a vertical resolution of 60 m at 8–20 km.

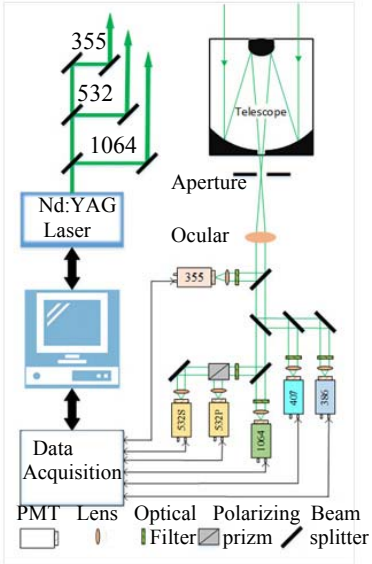

Fig. 1. Optical schematic of the Raman–Mie lidar system.

TABLE 1. Main Parameters of CALIOP and the Raman–Mie Lidar

Technical parameter	CALIOP value	Raman–Mie lidar value
Wavelength, nm	532/1064	355/532/1064
Single pulse energy, mJ	110	30
Repetition frequency, Hz	20.25	20
Telescope diameter, mm	1000	200
Vertical resolution, m	30–60	7.5
Horizontal resolution, m	333	–

Methods. The Mie scattering method is used to measure atmospheric aerosol, characterized by the backscattering coefficient and extinction coefficient [22–28]. The elastic scattering echo signal equation of lidar can be written as

$$P(z) = C[\beta_m(z) + \beta_a(z)]\exp\{-2\int_0^z [\alpha'_m(z') + \alpha'_a(z')]dz'\}\Big/ z^2, \quad (1)$$

where $P(z)$ represents the atmospheric backscattering signal at distance z, $P(z)\cdot z^2$ represents the lidar range-corrected signal, C is the device constant, $\alpha(z)$ is the atmospheric extinction coefficient at a distance from z, $\beta(z)$ represents the atmospheric backscattering coefficient at a distance from z, and the subscripts m and a respectively represent air molecules and aerosol particles. In this study, the ground-based lidar used the 532-nm wavelength signal, and the backscattered signal data were obtained by using Eq. (1) to obtain the range-corrected signal.

However, it is worth noting that the distance square correction signal of the ground-based fixed observation position is the key to joint space-borne and ground-based lidar observation [35]. On the one hand, it is because the ground-based lidar targets atmospheric aerosols, and the echo signal strength is positively correlated with aerosol content. At the same time, the range square correction signal can reduce the background noise signal. On the other hand, it is because at the boundary between the atmospheric boundary layer and the free atmosphere the aerosol concentration decreases very quickly. Such a result is reflected in the lidar echo signal, which is the rapid change of the lidar range-corrected signal profile, so the accuracy of the observation of aerosol change is higher by using the range-corrected signal.

Taking the first derivative of the distance squared correction signal of the above formula, the following formula is obtained:

$$\mathrm{DEV}(z) = d[P(z)z^2]/dz. \quad (2)$$

Here, the height corresponding to the minimum value of the DEV(z) profile is the height of the aerosol boundary layer [17, 29–31].

A large number of practical observations concluded that $\alpha(z)$ and $\beta(z)$ have the following relationship:

$$\alpha_a(z) = S_1\beta_a(z)^k, \quad (3)$$

where S_1 is an empirical constant, which is usually set as 50 sr, the constant k is typically 1.

Joint observation of typical weather cases. Data from observation points (31.90°N, 117.16°E) in the western suburbs of Hefei city were selected for effective joint observation with the satellite. When the CALIPSO satellite passed near Hefei, it screened and extracted the CALIOP aerosol data that could represent the period of the day in the western suburb of Hefei. Based on the data of the Raman–Mie lidar and CALIOP of the past two years, four typical types of weather were selected: sunny weather (less cloud, good air) on July 14, 2018; cloudy weather (good air, no haze) on September 10, 2018; moderate pollution weather (moderate haze, cloudless) on December 13, 2018; and severe pollution weather (heavy haze, cloudless) on January 20, 2019. When the satellite passed through Hefei, the backscattered vertical signal profiles of the four weather conditions were extracted (the total backscattered signal was extracted without considering multiple scattering), and the experimental observation data of the vertical signal profiles of distance correction of ground-based lidar were compared and analyzed jointly. Figure 2 shows the observation data of CALIOP and the Raman–Mie lidar. The observational results were verified by combining the $PM_{2.5}$ and PM_{10} concentration data (Fig. 3) of the Department of Ecology and Environment of Anhui Province (http://sthjt.ah.gov.cn/site/tpl/5371).

The red lines in Fig. 2 represent the data near the ground-based observation point when the CALIPSO satellite passes through. As can be seen from Fig. 2a, on July 14, 2018, the weather was clear and cloudless near the ground observation point, and the backscattering coefficient below 2 km was 2×10^{-3} km$^{-1}\cdot$sr^{-1} with a small amount of aerosol layer. The data from the meteorological department on that day showed that the air quality was excellent. According to Fig. 2b, on September 10, 2018, the weather near the ground observation point was clear and cloudy, with a thin layer of cloud at an altitude of 8 km, and the backscattering coefficient below 2 km was 8×10^{-4} km$^{-1}\cdot$sr^{-1}. The aerosol content was low, and the data from the meteorological department showed excellent air quality. According to Fig. 2c, on December 13, 2018, there were no clouds near the ground observation point, the backscattering coefficient below 1.5 km was 4×10^{-3} km$^{-1}\cdot$sr^{-1}, and there was a thick aerosol layer. The data from the meteorological department showed that the air quality was moderately polluted. It can be concluded from Fig. 2d that, on January 20, 2019, there were no clouds near the ground observation point, the backscattering coefficient below 2 km was 4.5×10^{-3} km$^{-1}\cdot$sr^{-1}, and there

was a thick aerosol layer. The data from the meteorological department showed that the air quality was seriously polluted.

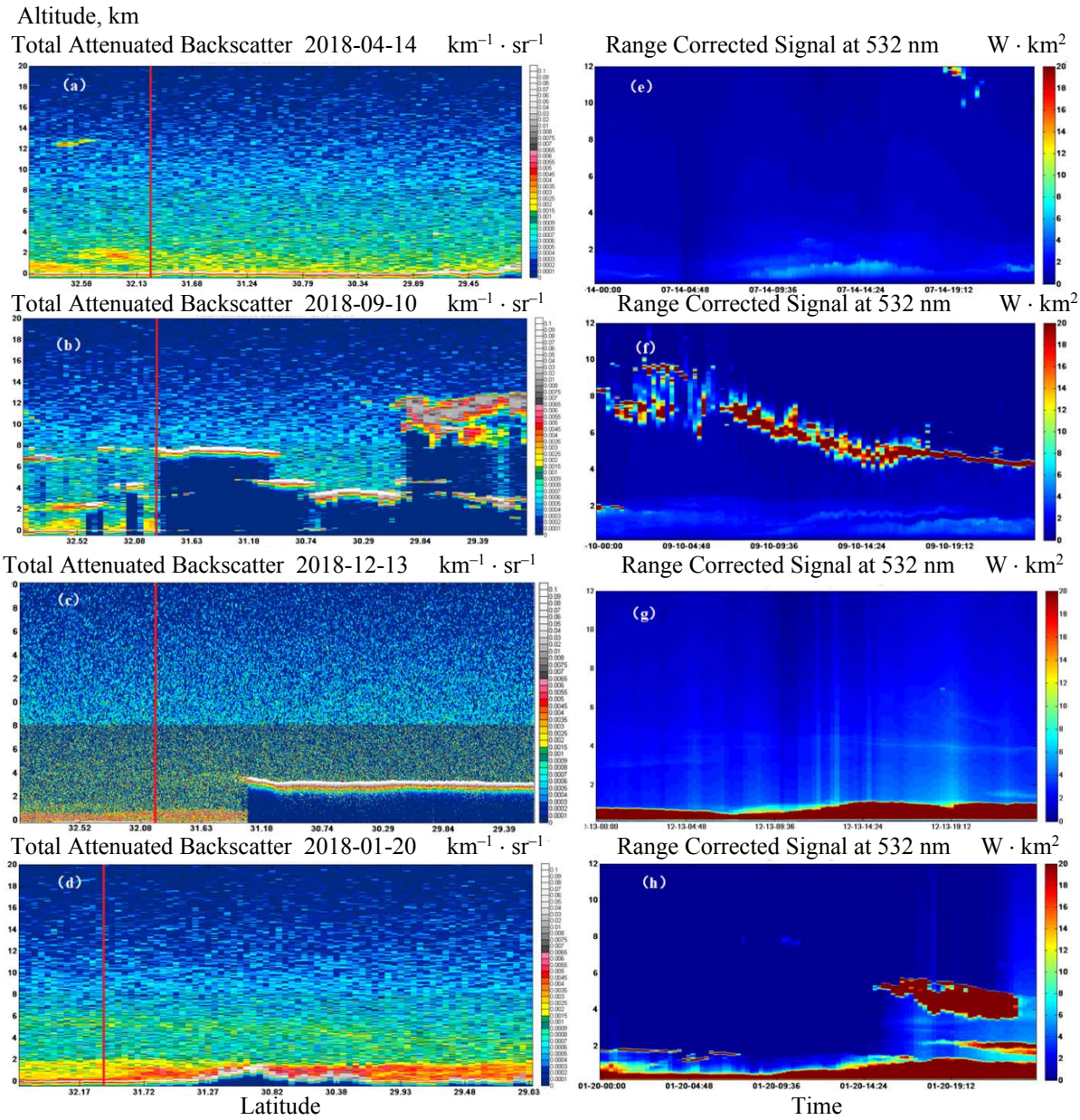

Fig. 2. Backscatter coefficient (km^{-1} · sr^{-1}) profile and range-corrected signal (W · km^2) of the Raman–Mie lidar: a, e) fine weather on July 14, 2018; b, f) cloudy weather on 10 September 2018; c, g) moderately polluted weather on 13 December 2018; d, h) severe pollution on January 20, 2019.

Case 1: On July 14, 2018, the weather in Hefei was sunny and the air quality was excellent. As can be seen from Fig. 2e, the range-corrected signal was 5 W·km^2 from 9 am to 2 pm below 2 km, and the weather was good at other times, with no cloud over the observation point on the day. According to Fig. 3a, the mass concentration of $PM_{2.5}$ on that day was below 30 μg/m^3, and that of PM_{10} was below 45 μg/m^3.

Case 2: On September 10, 2018, the weather in Hefei was cloudy and the air quality was excellent. As can be seen from Fig. 2f, the range-corrected signal was 4 W·km^2 below 2 km, and a thin layer of cloud appeared red from 6 km to 10 km above the observation point. It can be seen from Fig. 3b that the mass concentration of $PM_{2.5}$ on that day was below 35 μg/m^3, and the mass concentration of PM10 peaked at 8 am and 6 pm, respectively, at 74 and 73 μg/m^3.

Case 3: Hefei city experienced haze and moderate pollution on December 13, 2018. According to Fig. 2g, the range-corrected signal below 1.8 km was above 20 W·km^2, with a thick aerosol layer, and there was no cloud on the day above the observation point. According to Fig. 3c, the concentration of $PM_{2.5}$ and PM_{10} was highest in the early morning of that day, reaching 155 and 190 μg/m^3 respectively, before gradually decreasing, with the mass concentration reaching its lowest point at 16:30. It then rose slightly and reached a small peak at around 20:00. Note that PM_{10} meteorological data were missing in some periods.

Case 4: On January 20, 2019, Hefei suffered from heavy pollution due to haze weather. According to Fig. 2h, the range-corrected signal below 2 km was above 20 W·km^2, which was a thick aerosol layer. The sky above the observation point was red from 6 pm to 8 pm on that day from 4 km to 6 km, which was cloud. According to Fig. 3d, the concentration of $PM_{2.5}$ and PM_{10} maintained above 180 μg/m^3 from 0 am to 4 pm, then gradually decreased, and the mass concentration reached a minimum of 80 μg/m^3 at 24:00. Note that PM_{10} meteorological data were missing in some periods.

In general, based on comparisons of different pollution-level cases jointly observed by space-borne and ground-based lidar systems in the western YRDR, good performance is shown regarding the monitoring of different aerosol concentrations in the vertical distribution. In particular, the accuracy of the observations of changes in aerosol is becoming better by using the range-corrected signal, which can capture weather-scale heavy pollution processes effectively.

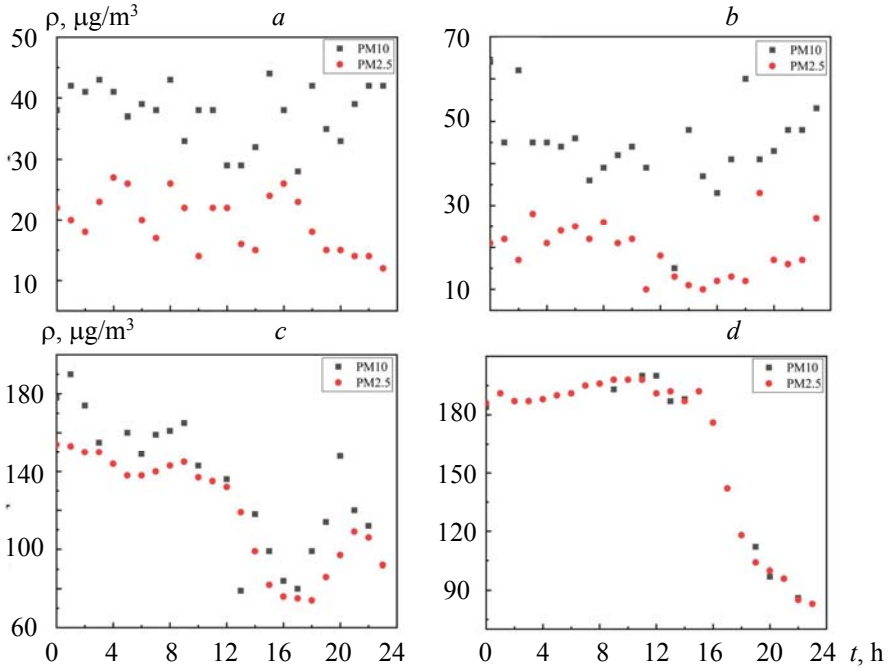

Fig. 3. Near-surface PM meteorological data: a) fine weather on July 14, 2018; b) cloudy weather on 10 September 2018; c) moderately polluted weather on 13 December 2018; d) severe pollution on January 20, 2019.

A heavy aerosol pollution case. Vertical observation. In view of the heavy pollution weather on January 20, 2019, continuous tracking observations were conducted. According to the data from the meteorological department, January 17, 2019 was sunny and the air quality was good. After that, mild pollution occurred on January 18 and 19, and severe pollution occurred on January 20. The pollution then decreased, and it was mild on January 21. January 22 was sunny and the air quality was good. Through continuous observation by the Raman–Mie lidar, the change in aerosol on January 17–22 above the observation point is shown in Fig. 4. The height line of the aerosol boundary layer in this pollution process was obtained by using the gradient method (Eq. (2)). From Fig. 5, it can be seen that the aerosol boundary layer was the lowest during the period of severe pollution from 22:00 on the night of the 19th to 04:00 on the morning of the 20th. The height of the aerosol boundary layer was less than 0.5 km, and in other periods was between 0.5 km and 2.2 km.

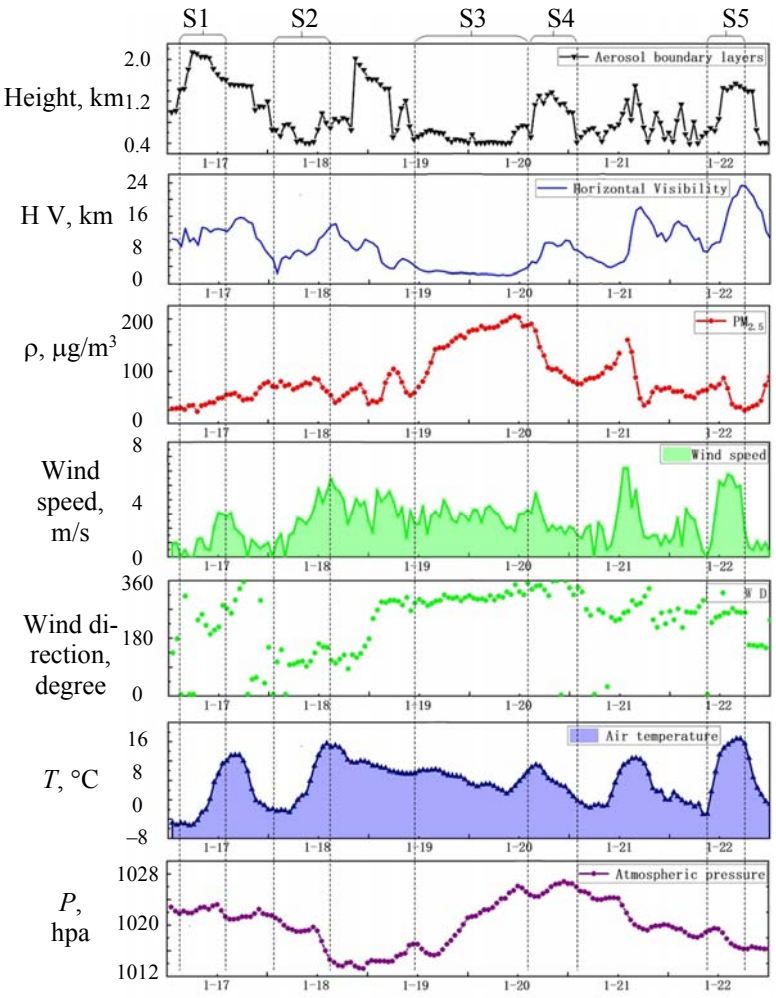

Fig. 4. Related influencing factors of the aerosol boundary layer. The relationship between aerosol boundary layer and horizontal visibility, $PM_{2.5}$ particle concentration, wind speed, wind direction, air temperature, and atmospheric pressure.

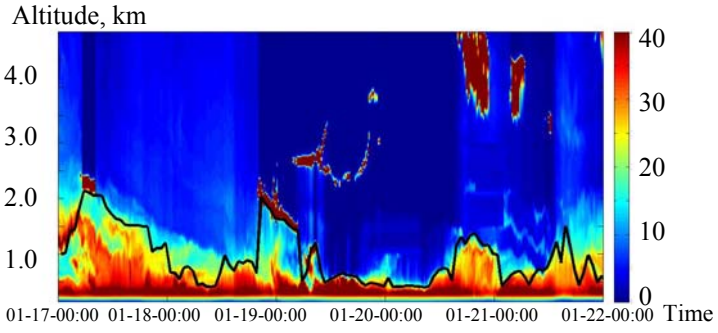

Fig. 5. Vertical profile of aerosol measured by ground-based lidar: aerosol change during the period from 00:00 on January 17 to 00:00 January 22, 2019.

Time series changes of surface $PM_{2.5}$ concentrations, boundary layer height and surface meteorological elements. The height values of the aerosol boundary layer were extracted and analyzed in combination with the visibility, $PM_{2.5}$ concentration value, wind speed, wind direction, air temperature, air pressure, and other related factors, as shown in Fig. 4.

In section S1, aerosol pollution had not occurred, the height of the aerosol boundary layer was between 1.2 and 2.2 km, the weather visibility was about 10 km, the concentration of $PM_{2.5}$ particles was about 50 μg/m^3, the wind speed was about 1 m/s, the wind direction changed greatly, the temperature raised gradually between 4 and 9°C, and the air pressure fluctuated slightly at 1022 hPa.

In section S2, aerosol pollution began to occur, the height of the aerosol boundary layer dropped below 0.8 km, resulting in the visibility dropping to 8.8 km. However, at this time, the concentration of $PM_{2.5}$ particles in the section was not high, being about 75 μg/m^3, and the wind speed was below 5 m/s. It was warm air blown by the southeast wind. The highest temperature rose to 12°C, and the air pressure fluctuated slightly at 1021 hPa. In section S3, pollution was caused by local accumulation. The height of the aerosol boundary layer dropped to its lowest, and the visibility in this section was about 4 km. Due to the decrease in the boundary layer and the wind speed at about 3 m/s being a weak, still wind, there was a sharp increase in the concentration of $PM_{2.5}$ particles, reaching a peak of about 200 μg/m^3 and resulting in severe pollution. In this period, the wind direction was a northwest wind blowing the cold air. Due to the decreased boundary layer, surface atmospheric radiation was strengthened, the air temperature reversed slightly, and the air pressure rose to 1026 hPa. At the crossing of cold air in section S4, a value of 1.5 km appeared in the boundary layer.

At this point, the vertical mixing intensified in section S5, and the concentration of $PM_{2.5}$ particles dropped to 60 μg/m^3. Atmospheric radiation weakened, the temperature dropped to 0°C, and the pressure fluctuated slightly at 1024 hPa. Section S5 was characterized by the cleaning process of pollutants. The boundary layer rose to 1.6 km, so the visibility rose to 22 km, the concentration of $PM_{2.5}$ particles dropped below 60 μg/m^3, the southwest wind blew cold air, the wind speed gradually increased to 6 m/s, the temperature gradually rose to 12°C, and the air pressure dropped.

Table 2 shows the average visibility data, the daily maximum value of $PM_{2.5}$, and the maximum value of relative humidity during the pollution process. It can be seen that, on the day of severe pollution, the concentration value of $PM_{2.5}$ increased significantly, the daily average visibility value decreased, and the relative humidity value decreased.

TABLE 2. Related Factors Data during the Period of Pollution

Date/time	Average daily visibility, m	Maximum $PM_{2.5}$, μg/m^3	Maximum relative humidity, %
2019.01.17/00:00–23:00	11969.79	79	96
2019.01.18/00:00–23:00	8795	86	98
2019.01.19/00:00–23:00	3983.375	175	89
2019.01.20/00:00–23:00	4922.5	206	91
2019.01.21/00:00–23:00	9136.625	160	89
2019.01.22/00:00–23:00	14712.96	89	92

Backward trajectory analysis of the pollution process. In order to determine the properties of aerosol particle pollutants, CALIOP and Raman–Mie lidar particle depolarization ratio data were extracted separately, as shown in Fig. 6. It can be seen that the satellite- and earth-lidar observational results were relatively consistent. The depolarization ratio of aerosol particles was less than 0.15, which may have been a mixture of fine particles of industrial exhaust, dust, automobile exhaust.

In order to determine the source of aerosol pollutants, the HYSPLIT model provided by NOAA was used to analyze the backward trajectory of aerosol particles in the five aerosol structure layers at 100, 300, 500, 1000, and 2000 m (Fig. 7).

It can be seen that the aerosol particles at the heights of 100 and 300 m originated from the territory of Mongolia and passed through the Beijing–Tianjin–Hebei region of China. The altitude drops all the way from 3500 m, and finally sinks to the Hefei area after following the mixing of cold air from the northwest and north directions. The aerosol particles within 500 m were from the Beijing–Tianjin–Hebei region, and the aerosol particles within 1000 and 2000 m were from Mongolia. The aerosol particles following the cold air at 500 and 2000 m arrived over Hefei in the northern and northwestern direction, successively. Its transmission process first experienced a rise and then a sink. However, the aerosol particles at 1000 m reached the airspace over Hefei in the northwest after descending and then climbing. During the period of the 19 and 20th, different types of aerosol particles were violently mixed in the airspace over Hefei, forming heavy pollution.

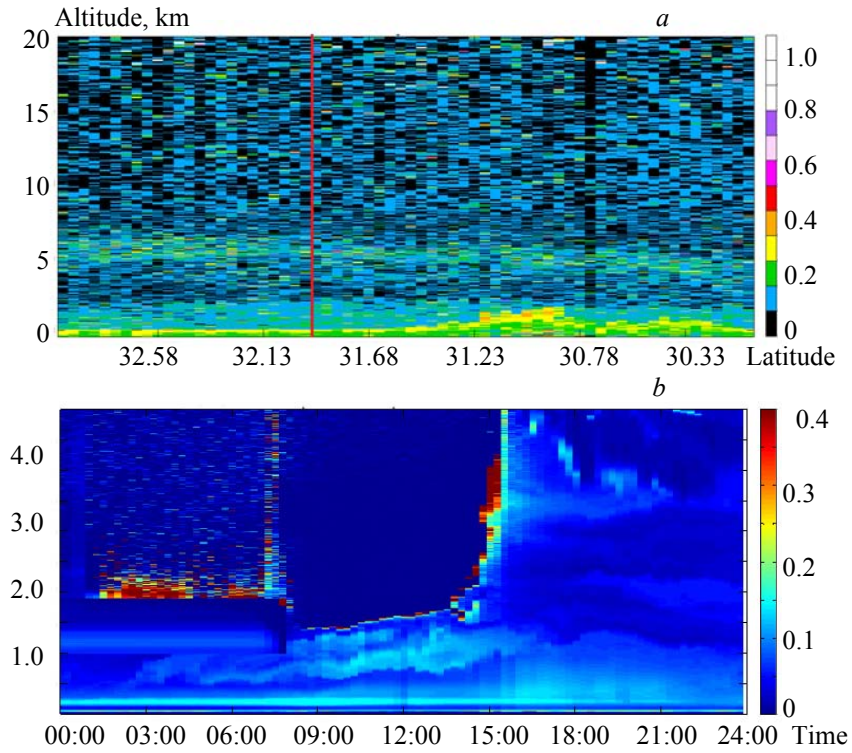

Fig. 6. Depolarization ratio of aerosol particles: a) CALIOP depolarization ratio of aerosol particles; b) depolarization ratio of Raman–Mie lidar aerosol particles.

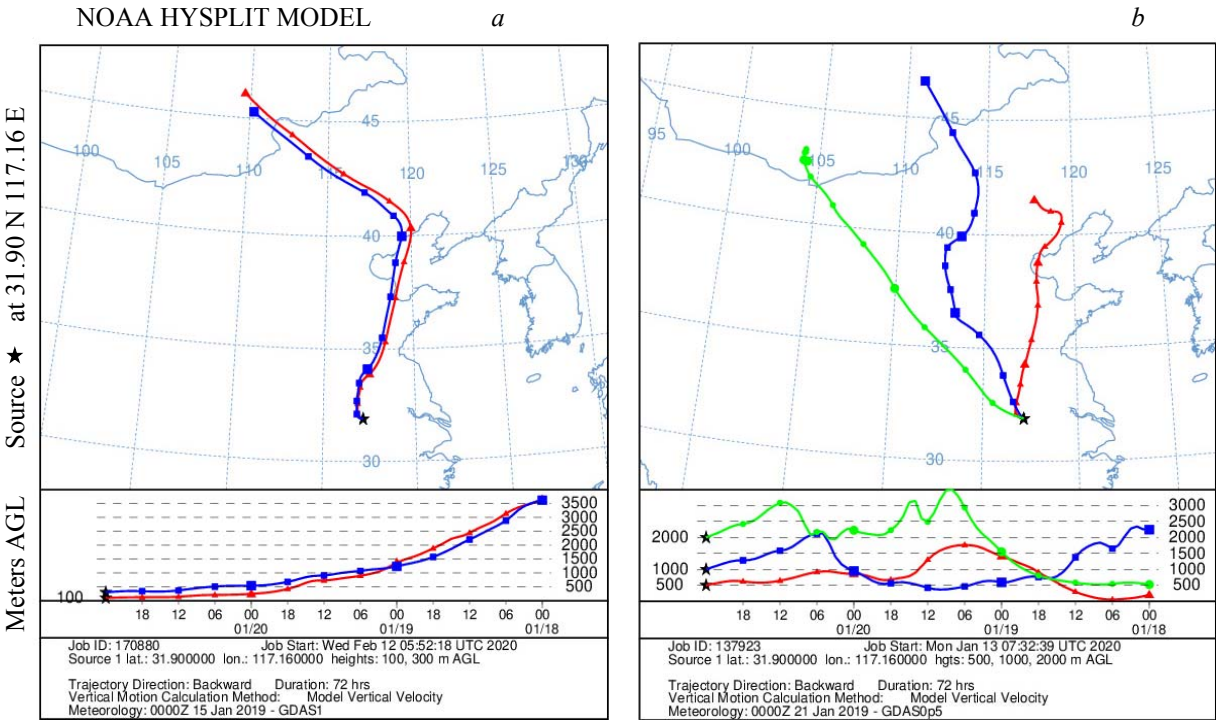

Fig. 7. Backward trajectory of pollutants from the HYSPLIT model, backward trajectories ending at 00:00 UTC 21 Jan 19 Meteorological Data GDAS (a), and GFSG (b).

Conclusions. Four typical weather cases in the Hefei area in the past two years were observed by the space-borne CALIOP and Raman–Mie lidars, and the pollution process on January 17–22, 2019 was continuously observed and tracked. The conclusions are as follows.

The analysis of four typical weather cases showed that the results of the vertical backscatter profile of the satellite-borne CALIOP and the vertical profile of the ground-based lidar vertical range-corrected signal were basically the same, indicating the effectiveness and accuracy of satellite-ground lidar joint observation.

Through continuous fixed-point observation of the pollution process and calculation of the aerosol boundary layer obtained by the gradient method, it can be concluded that the aerosol boundary layer was the lowest (less than 500 m) during the period of severe pollution from 22:00 on January 19th to 04:00 on January 20th, and the boundary layer height ranged from 500 m to 2.2 km during the rest of the period.

We extracted the height of the aerosol boundary layer and compared it with near-ground data. It can be concluded that the height of the aerosol boundary layer was closely related to the $PM_{2.5}$ concentration, wind speed, wind direction, air temperature, air pressure, relative humidity, and other factors, which interacted and influenced each other. The aerosol boundary layer height and $PM_{2.5}$ concentration were negatively correlated, while the aerosol boundary layer height and horizontal visibility were positively correlated.

By studying the depolarization ratio of aerosol and the traceability analysis of the HYSPLIT pattern, it was found that the depolarization ratio of aerosol particles of this pollutant was less than 0.15, and the pollution source was mainly aerosol particles blown from the north, which were caused by the intensified mixing of local pollutants.

Our findings provide scientific observational evidence towards a better understanding of the vertical distribution of aerosol and its spatial variations. Obtaining the correlation characteristics of aerosol vertical distributions is of great significance for urban weather change. This paper highlights that the relationship between aerosol-related characteristics, the atmospheric boundary layer height and $PM_{2.5}$ concentration changes offers useful supporting data for the study of weather changes and the prevention of pollution.

Acknowledgments. We would like to thank the Key Laboratory of Atmospheric Optics, the Anhui Institute of Optics and Fine Mechanics, the NASA (https://eosweb.larc.nasa.gov/content/calipso-search-and-subset-tool), the ministry of environmental protection of the People's Republic of China, and NOAA (https://ready.arl.noaa.gov/hypub-bin/trajasrc.pl) for providing ground-based lidar data, spaceborne data, backward trajectory data, and meteorological data, respectively. The authors declare no competing financial interest. We thank Professor Yuanjian Yang of Nanjing University of Information Science and Technology for writing the paper.

This work was jointly funded by the Strategic Priority Research Program of Chinese Academy of Sciences (Grant No. XDA17040524) and Key Program of 13th five-year plan, CASHIPS, Grant No. KP-2019-05).

REFERENCES

1. T. L. Anderson, R. J. Charlson, S. E. Schwartz, et al., *Science*, **300** (5622) 1103–1104 (2003).
2. J. M. Ge, J. Su, T. P. Ackerman, Q. Fu, et al., *J. Geophys. Res.*, **115**, D00K12 (2010).
3. U. Burkhardt, B. Karcher, U. Schumann, *Bull. Am. Meteorol. Soc.*, **91**, No. 4, 479 (2010).
4. Y. Yang, Z. Zheng, S. H. L. Yim, M. Roth, G. Ren, Z. Gao, T. Wang, Q. Li, C. Shi, G. Ning, Y. B. Li, *Geophys. Res. Lett.*, **47**, No. 1 (2020), doi:10.1029/2019gl084288.
5. J. H. Seinfeld, S. N. Pandis, *Environment*, **52**, 6 (1998).
6. E. Saikawa, V. Naik, L.W. Horowitz, J. Liu, D. L. Mauzerall, *Atm. Environ*., **43**, 2814–2822 (2009).
7. C. Lin, Y. Li, A. K. Lau, X. Deng, T. K. Tse, J. C. Fung, C. Li, Z. Li, X. Lu, X. Zhang, et al., *Remote Sens. Environ.*, **179**, 13–22 (2016).
8. X.-W. Zeng, E. Vivian, K. A. Mohammed, S. Jakhar, M. Vaughn, J. Huang, A. Zelicoff, P. Xaverius, Z. Bai, S. Lin, et al., *Atm. Environ*., **138**, 144–151 (2016).
9. M. Zhong, F. Chen, E. Saikawa, *Environ. Int*., **123**, 256–264 (2019).
10. J. Guo, X. Zhang, C. Cao, et al., *Intern. J. Remote Sens.*, **31**, No. 17-18, 4743–4755 (2010).
11. Weifeng Wang, Jie Yu, Yang Cui; Jun He; Peng Xue, Wan Cao, Hongmei Ying, Wenkang Gao, Yingchao Yan, Bo Hu, Jinyuan Xin, Lili Wang, Zirui Liu, Yang Sun, Dongsheng Ji, Yuesi Wang, *Atm. Res.*, 105–117 (2018).
12. Qun Wang, Nan Jiang, Shasha Yin, Xiao Li, Fei Yu, Yue Guo, Ruiqin Zhang, *Atm. Res.*, 1–11 (2017).
13. Y. Hua, Z. Cheng, S. Wang, J. Jiang, D. Chen, S. Cai, X. Fu, Q. Fu, C. Chen, B. Xu, et al., *Atm. Environ*., **123**, 380–391 (2015).

14. J. P. Guo, X. Y. Zhang, Y. R. Wu, Y. Z. Zhaxi, H. Z. Che, B. La, W. Wang, X.W. Li, *Atm. Environ.*, **45** (37), 6802–6811 (2011).
15. J. P. Guo, J. He, H. L. Liu, Y. C. Miao, H. Liu, P. M. Zhai, *Atm. Environ*., **140**, 311–319 (2016).
16. Y. Yang, X. Zheng, Z. Gao, H. Wang, T. Wang, Y. Li, G. N. C. Lau, S. H. L. Yim, *J. Geophys. Res. Atm*., **123**, 10–991 (2018).
17. J. Wang, G. De Leeuw, S. Niu, H. Kang, *Remote Sens*., **11**, 1696 (2019).
18. C. Xing, C. Liu, S. Wang, K. L. Chan, Y. Gao, X. Huang, W. Su, C. Zhang, Y. Dong, G. Fan, et al., *Atm. Chem. Phys. Discuss*., **17**, 14275–14289 (2017).
19. C. Shi, R. Yuan, B. Wu, Y. Meng, H. Zhang, Z. Gong, *Sci. Total Environ*., **642**, 1221–1232 (2018).
20. H. Kang, B. Zhu, J. Gao, Y. He, H. Wang, J. Su, C. Pan, T. Zhu, B. Yu, *Atm. Chem. Phys.*, **19**, 3673–3685 (2019), doi: 10.5194/acp-19-3673-2019.
21. Y. Yang, S. Yim, J. Haywood, M. Osborne, J. Chan, Z. Zeng, J. Cheng, *J. Geophys. Res. Atm.*, **124**, No. 16, 9609–9623 (2019), doi: 10.1029/2019JD031140
22. S. Lolli, L. P. D'Adderio, J. R. Campbell, M. Sicard, E. J. Welton, A. Binci, J. M. Baldasano, *Remote Sens.*, **10**, No. 7, 1102 (2018).
23. S. Lolli, W. Y. Khor, M. Z. Matjafri, H. S. Lim, *Remote Sens.*, **11**, 2660 (2019).
24. G. Pappalardo, U. Wandinger, L. Mona, et al., *J. Geophys. Res. Atm.*, **115** (2010).
25. D. Wu, Z. Wang, B. Wang, et al., *Appl. Phys. B - Lasers and Optics*, **102**, No. 1, 185–195 (2011).
26. R. R. Rogers, C. A. Hostetler, J. W. Hair, et al., *Atm. Chem. Phys.*, **11**, No. 3, 1295–1311 (2011).
27. J. F. Barlow, T. M. Dunbar, E. G. Nemitz, et al., *Atm. Chem. Phys.*, **11**, 2111–2125 (2011).
28. D. L. Hlavka, J. E. Yorks, S. A. Young, et al., *J. Geophys. Res. Atm.*, **117**(D09207) (2012).
29. J. Guo, M. Lou, Y. Miao, et al., *Environ. Poll.*, **230**, 1030–1039 (2017).
30. K. Qin, L. Wu, M. S. Wong, et al., *Atm. Environ.*, **141**, 20–29 (2016).
31. T. Su, J. Li, C. Li, P. Xiang, K. H. Lau, J. Guo, et al., *J. Geophys. Res.: Atmospheres*, **122**, No. 7, 3929–3943 (2017).
32. T. N. Su, Z. Q. Li, R. Kahn, *Atm. Chem. Phys*., **18**, No. 21, 15921–15935 (2018).
33. C. Shi, I. C. Nduka, Y. Yang, Y. Huang, R. Yao, H. Zhang, B. He, C. Xie, Z. Wang, S. H. L. Yim, *Atm. Environ.*, **223**, 117239 (2020).
34. D. Liu, Y. Yang, Z. Cheng, H. Huang, B. Zhang, T. Ling, Y. Shen, *Opt. Express*, **21**, 13084–13093 (2013).
35. Songlin Fu, Chenbo Xie, Peng Zhuang, et al., *Atmosphere*, **10**, 656 (2019).